Journal of Geophysical Research: Solid Earth

RESEARCH ARTICLE
10.1002/2017JB015158

Key Points:
- Maximum horizontal stress orientations rotate from a regional trend of ~N60°E to ~E/W near the New Madrid and Wabash Valley Seismic Zones
- Localized reverse-faulting stress regime in the New Madrid and Wabash Valley Seismic Zones deviates from regional strike-slip stress regime
- We objectively solve for the spatial smoothing parameter, data uncertainties, and selection of the focal mechanism nodal planes

Supporting Information:
- Supporting Information S1

Correspondence to:
G. Carlson,
gacarls1@asu.edu

Citation:
Carlson, G., Johnson, K., Chuang, R., & Rupp, J. (2018). Spatially varying stress state in the central U.S. from Bayesian inversion of focal mechanism and in situ maximum horizontal stress orientation data. *Journal of Geophysical Research: Solid Earth*, *123*, 3871–3890. https://doi.org/10.1002/2017JB015158

Received 1 NOV 2017
Accepted 29 MAR 2018
Accepted article online 6 APR 2018
Published online 8 MAY 2018

Spatially Varying Stress State in the Central U.S. From Bayesian Inversion of Focal Mechanism and In Situ Maximum Horizontal Stress Orientation Data

Grace Carlson[1,2], Kaj Johnson[1], Ray Chuang[3], and John Rupp[4]

[1]Department of Earth and Atmospheric Sciences, Indiana University, Bloomington, IN, USA, [2]Now at School of Earth and Space Exploration, Arizona State University, Tempe, AZ, USA, [3]Department of Geography, National Taiwan University, Taipei, Taiwan, [4]Indiana Geological and Water Survey, Bloomington, IN, USA

Abstract The crustal stress state in the Midcontinent of the United States has been a focus of research for many years due to anomalously high rates of seismicity in the region. This interest is recently renewed because of ongoing wastewater injection and CO_2 sequestration in the Illinois Basin and its potential to induce seismicity. When fluid is injected, pore pressure increases, decreasing effective normal stress and increasing the potential for faults optimally oriented with respect to the direction of maximum compressive stress to slip. In order to better manage this risk, we present a study on the spatial distribution of principal stress orientations in the Illinois Basin and surrounding region using focal mechanism solutions and in situ measured maximum horizontal stress orientation indicators from borehole breakout, core fracture, overcoring, hydraulic fracture, and strain gauge measurements. To invert these data for the deviatoric stress tensor, we extend the damped-least stress inversion of Hardebeck and Michael (2006, https://doi:10.1029/2005JB004144) with the mixed linear/nonlinear Bayesian inversion scheme of Fukuda and Johnson (2010, https://doi:10.1111/j.1365-246X.2010.04564.x). The stress inversion provides an objective means to estimate nonlinear parameters including the spatial smoothing parameter, unknown data uncertainties, and selection of focal mechanism nodal planes. Results indicate a systematic rotation of the maximum horizontal stress orientation (S_{Hmax}) across a 1,000-km width of the Midcontinent. S_{Hmax} rotates from ~N60°E to ~E/W orientation across the southern Illinois Basin. The principal stress orientations are largely consistent with the observed pattern of strike-slip faulting and reverse faulting near the New Madrid and Wabash Valley Seismic Zones.

1. Introduction

Stress in intraplate regions is thought to be relatively homogenous and diffuse with maximum horizontal stress generally oriented coincident with the direction of absolute plate motion (Zoback, 1992; Zoback & Zoback, 1980, 1989). Because of the stability of continental interiors, we would expect to find few regions of active seismicity. The New Madrid Seismic Zone and nearby Wabash Valley and St. Genevieve Seismic Zones located in the middle of the North American plate defy this assumption (Figure 1). This region has generated large historic earthquakes and continues to experience high rates of seismicity despite its location far from any active plate boundary.

For this study, we focus on an area in the Midcontinent of the United States containing the Illinois and western Appalachian basins (Figure 1a) and the New Madrid Seismic Zone, Wabash Valley Seismic Zone, and St. Genevieve Seismic Zone (Figure 1b). In the New Madrid Seismic Zone, crystalline basement faults are associated with the Reelfoot Rift, a Cambrian-aged failed rift system that has experienced Holocene reactivation. Seismicity in this zone occurs along steeply dipping, northeast trending faults reactivated in a right-lateral strike-slip sense with a northwest trending compressional step-over experiencing reverse faulting (Csontos & Van Arsdale, 2008; Gomberg, 1992, 1993). Multiple Mw 7+ events have been documented from paleoliquefaction studies and historical records (Kelson et al., 1996; Tuttle & Schweig, 1996). The most notable of these events occurred in a sequence of Mw 7–8 earthquakes in 1811–1812 causing severe ground shaking and damage to communities residing in the Midcontinent (Johnston & Schweig, 1996; Tuttle, 2001; Tuttle & Schweig, 1996). In close proximity to the New Madrid Seismic Zone is the Wabash Valley Seismic Zone, located in southeastern Illinois. The Wabash Valley Seismic Zone has produced numerous Mw 5+ earthquakes with the most recent occurring in 1968, 1987, and 2008 (Hamburger et al., 2011; Hamburger &

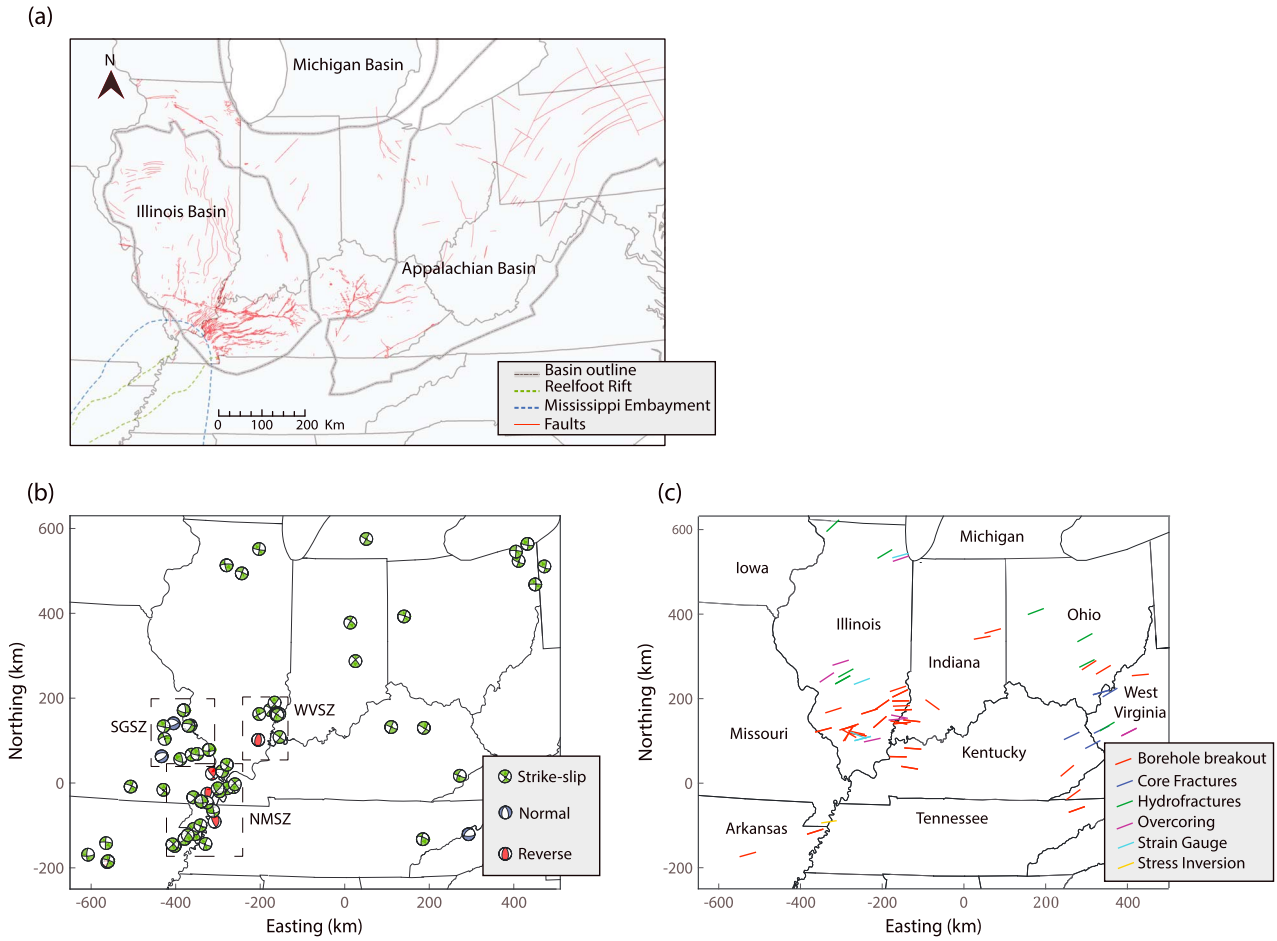

Figure 1. Study area and locations of focal mechanisms and in situ orientation indicators used in the inversion. (a) Study area including sedimentary basins and faults. Also shown is an outline of the Reelfoot Rift located in the modern Mississippi River Embayment (adapted from Lahann et al., 2017). (b) Locations of focal mechanisms used in the study. The color represents faulting style: red shows reverse faulting, green strike-slip, and blue normal faulting. The dashed boxes show approximate outlines of the New Madrid Seismic Zone (NMSZ), the Wabash Valley Seismic Zone (WVSZ), and the St. Genevieve Seismic Zone (SGSZ). (c) In situ maximum horizontal stress orientation indicators. The colors represent different sources. The red colors are borehole breakouts, the dark blue colors are from core fractures, the green colors are hydrofractures, the purple colors are found from overcoring, the light blue colors are found using strain gauges, and the yellow color shows orientation from Hurd and Zoback (2012a) stress inversion.

Rupp, 1988; Nuttli, 1979). Faults in this zone also extend into the Precambrian basement and are reactivated as strike-slip and reverse faulting earthquakes (Bear, 1998; Pavlis et al., 2002). Both zones continue to produce Mw 3–5 seismic events. In the St. Genevieve Seismic Zone, strike-slip faulting occurs along northwest trending faults (Nelson, 1991; Yang et al., 2014).

The goal of this study is to evaluate the stress state in the Midcontinent by examining faulting style and orientation of maximum horizontal stress (S_{Hmax}). A number of studies have examined the contemporary state of stress in the Midcontinent using borehole breakout measurements (Mazzotti & Townend, 2010; Zoback & Zoback, 1989); focal mechanism *P* axis (Hurd & Zoback, 2012a, 2012b; Zoback, 1992; Zoback & Zoback, 1980); other in situ measurements such as overcoring, core fractures, hydrofractures, and field observations such as dike intrusions and slickensides (Zoback & Zoback, 1980, 1989); and formal focal mechanism inversions (Hurd & Zoback, 2012a; Mazzotti & Townend, 2010). These studies have found a regional NE-SW orientation of maximum compressive stress in the Midcontinent (Zoback & Zoback, 1980) with slight rotations near the New Madrid Seismic Zone to ENE-WSW (Hurd & Zoback, 2012b; Mazzotti & Townend, 2010) and a nearly E-W rotation near the Wabash Valley Seismic Zone (Hurd & Zoback, 2012a; Mazzotti & Townend, 2010). Additionally, some work has been done to characterize the relative magnitudes of principal stresses in the Midcontinent, finding that S_{Hmax} is generally greater than the vertical stress (S_v), which is greater than the minimum horizontal stress (S_{hmin}) except in the region surrounding the New Madrid

Seismic Zone, which shows S_v nearly equal to S_{hmin} (Hurd & Zoback, 2012a). Analyses of maximum compressive stress orientations have often focused either on regional orientations or on particular seismic zones. In this study, we jointly invert focal mechanisms and in situ orientations both within and outside of the three major midcontinent seismic zones to show how the orientation of maximum compressive stress varies within and surrounding these regions. We show that S_{Hmax} is oriented ENE-WSW across the Midcontinent, with the largest deviations found in the Wabash Valley Seismic Zone and western Kentucky, where the orientation of maximum compressive stress rotates to approximately E-W. We expand on the work done by the previous studies to show that in the northern New Madrid Seismic Zone as well as in the Wabash Valley Seismic Zone, there exists highly concentrated zones of compression, where we find a reverse faulting stress regime, and the relative values of S_{hmin} and S_v are nearly equal.

The local heterogeneities in maximum horizontal stress orientation are of particular importance to this study area because several formations in the Illinois Basin (Figure 1a), a Paleozoic sedimentary basin filled with layers of sandstones, limestones, and shales, are used to store large volumes of supercritical CO_2, with more sites being considered (Lahann et al., 2017). There is also ongoing wastewater injection associated with oil and gas production. Seismicity with the subsurface storage of fluids has been of concern recently (e.g., Chang & Segall, 2016; Keranen et al., 2013; Kim, 2013; Yeck et al., 2016; van der Baan & Calixto, 2017). Induced microseismic events caused by CO_2 sequestration have been documented in this region by Kaven et al. (2015) and Couëslan et al. (2014) in Illinois and from wastewater injection by Kim (2013) in Ohio. Understanding the stress regime in this region is important in order to mitigate the risk of fault reactivation. In areas where faults are optimally oriented with respect to the direction of maximum compressive stress, enhancing pore pressure through fluid injection decreases the effective normal stress and increases the potential for fault failure (Zhang et al., 2013). An understanding of the stress field in addition to fault orientations will help determine which faults may be subject to reactivation under increased pore pressures.

In this paper, we examine the degree of spatial heterogeneity in the midcontinent stress field by solving for a spatially variable stress field with optimized smoothing. We extend the damped-least stress inversion method of Hardebeck and Michael (2006) and solve for the stress field across a regular grid. As with most stress inversion methods, the method used in this investigation is dependent on the assumption that faults slip parallel to the orientation of maximum shear stress, known as the "Wallace-Bott hypothesis" (Bott, 1959; Wallace, 1951). A significant obstacle in many stress inversion methods involving focal mechanism solutions is in the choice of the fault plane and associated slip vector. Earthquake focal mechanisms do not differentiate between the fault plane, where slip takes place, and the auxiliary plane. This method works to constrain the choice of the fault plane, thus creating a stress map with a better fit to the data and lower misfit angles between computed shear stress and observed slip directions.

2. Data

We compiled focal mechanism solutions from the Saint Louis University North America Moment Tensor catalog (Herrmann et al., 2011), the Global-Centroid-Moment Tensor catalog (Ekström et al., 2012), and the OIINK Catalog (Yang et al., 2014). A detailed list of the focal mechanism solutions and references for each data set can be found in Table 1. The focal mechanisms are plotted in Figure 1b. The second data set was generated from in situ measurements of maximum horizontal stress orientation compiled by Lahann et al. (2017) from various sources (Indiana Geological and Water Survey, 2015; Mazzotti & Townend, 2010; World Stress Map, 2015). This data set includes 57 orientations from borehole breakout, core fracture, overcoring, hydraulic fracture, and strain gauge measurements, and one from a formal stress inversion by Mazzotti and Townend (2010) (Figure 1c). Originally, we planned to separate the in situ measurements and objectively solve for relative weighting of each type as in Fukuda and Johnson (2010). This produced an unstable result due to the small size and spatial distribution of the individual in situ data sets so we resorted to combining them in to one. The types of in situ orientation measurements used in this study are often given quality rankings of A–E (e.g., World Stress Map, 2015), with A being the most reliable and E being the least reliable. Where quality rankings are provided, such as the orientations from the World Stress Map, only measurements with quality rankings A–C are used. A summary of the in situ orientation data is presented in Table 2.

Table 1
Focal Mechanism Solutions

Latitude (°N)	Longitude (°E)	Depth (km)	Mw	Strike (°)	Dip (°)	Rake (°)	Catalog	Date (day-month-year)
36.37	−89.51	8	4.23	350	84	145	SLU	2-Feb-1962
36.64	−90.05	15	4.66	304	78	−28	SLU	3-Mar-1963
37.22	−89.31	2	3.6	280	70	−20	SLU	14-Aug-1965
37.48	−90.94	5	4.6	260	40	−70	SLU	21-Oct-1965
37.44	−90.44	15	4.04	350	60	135	SLU	21-Jul-1967
37.91	−88.37	22	5.29	0	46	79	SLU	9-Nov-1968
35.86	−89.95	16	4.1	220	75	150	SLU	17-Nov-1970
41.6	−89.4	13	4.12	170	70	160	SLU	15-Sep-1972
35.8	−84	13	4.08	190	70	150	SLU	30-Nov-1973
38.55	−88.07	15	4.34	310	70	0	SLU	3-Apr-1974
36.54	−89.68	9	3.74	85	60	−20	SLU	13-Jun-1975
35.59	−90.48	16	4.23	45	80	−150	SLU	25-Mar-1976
38.2	−84.79	15	5	203	90	180	GCMT	26-Jul-1976
38.17	−83.91	12	5.04	30	60	180	SLU	27-Jul-1980
35.17	−92.21	6	4.38	330	60	55	SLU	21-Jan-1982
41.64	−81.11	15	5	113	72	6	GCMT	30-Jan-1982
40.55	−84.39	4	4.4	20	80	−170	SLU	12-Jul-1986
38.71	−87.95	10	4.96	135	70	15	SLU	10-Jun-1987
37.16	−89.58	15	4.28	140	75	50	SLU	26-Sep-1990
36.56	−89.83	8	4.13	90	67	20	SLU	4-May-1991
37.36	−89.19	16	3.85	30	70	170	SLU	5-Feb-1994
35.97	−90	11	3.78	120	65	−15	SLU	29-Nov-1996
41.49	−80.39	2	4.47	110	70	20	SLU	25-Sep-1998
41.99	−80.83	2	3.85	5	79	159	SLU	26-Jan-2001
35.19	−92.19	5	4.34	20	85	−165	SLU	4-May-2001
37.98	−87.8	17	4.49	125	90	10	SLU	18-Jun-2002
36.89	−88.99	5	4.02	165	85	15	SLU	6-Jun-2003
36.8	−91.72	5	3.71	25	80	−165	SLU	16-Aug-2003
38.49	−87.86	26.9	5.4	295	88	1	GCMT	17-Apr-2004
38.48	−87.91	21.8	4.8	305	84	5	GCMT	17-Apr-2004
36.73	−89.68	2	3.49	175	55	70	SLU	15-Jun-2004
41.44	−88.96	7	4.15	20	90	−165	SLU	28-Jun-2004
36.86	−89.16	5	3.46	140	70	20	SLU	16-Jul-2004
39.61	−85.75	13	3.83	320	75	15	SLU	12-Sep-2004
35.75	−90.23	14	4.11	55	80	−165	SLU	10-Feb-2005
35.83	−90.15	8	4.22	315	60	20	SLU	1-May-2005
36.14	−89.46	15	3.89	155	65	70	SLU	2-Jun-2005
36.95	−88.96	4	3.6	320	80	15	SLU	20-Jun-2005
35.88	−82.8	8	3.65	90	60	−60	SLU	25-Aug-2005
41.84	−81.17	4	3.55	275	75	0	SLU	20-Jun-2006
38.1637	−90.2064	14.37	1.79	32.64	58.08	−156.68	OIINK	19-Aug-2007
37.5451	−90.141	5.59	1.58	234.1	84.08	178.18	OIINK	7-Sep-2007
38.1541	−90.2605	10.26	1.96	281.82	60.62	−36.98	OIINK	28-Sep-2007
38.1928	−90.6663	9.82	1.99	294.05	37.28	−49.33	OIINK	4-Oct-2007
37.8518	−90.8852	9.71	1.76	250.33	55.1	−1.4	OIINK	20-Feb-2008
37.6638	−89.6873	0.13	2.03	88.59	70.57	3.08	OIINK	27-Feb-2008
37.5673	−89.993	8.27	1.91	98.57	74.13	28.28	OIINK	3-Mar-2008
38.48	−87.89	14	4.61	225	80	−180	SLU	18-Apr-2008
38.45	−87.89	14	5.23	25	90	−175	SLU	18-Apr-2008
38.47	−87.82	15	4	210	85	175	SLU	21-Apr-2008
38.45	−87.87	13	3.72	295	80	5	SLU	25-Apr-2008
38.48	−90.41	19	2.75	105	60	30	SLU	5-May-2008
38.45	−87.87	17	3.37	215	70	180	SLU	5-Jun-2008
41.97	−88.49	11	3.8	100	80	5	SLU	10-Feb-2010
36.79	−89.36	5	3.37	305	45	5	SLU	2-Mar-2010
40.43	−85.89	14	3.82	305	65	10	SLU	30-Dec-2010
38.12	−90.93	27	3.86	100	80	25	SLU	7-Jun-2011
41.12	−80.68	3	3.69	270	85	−10	SLU	31-Dec-2011
36.85	−89.41	8	3.86	150	45	25	SLU	21-Feb-2012
37.13	−82.98	14	4.16	110	85	−30	SLU	10-Nov-2012

Table 1 *(continued)*

Latitude (°N)	Longitude (°E)	Depth (km)	Mw	Strike (°)	Dip (°)	Rake (°)	Catalog	Date (day-month-year)
35.62	−90.54	10	3.67	315	75	−5	SLU	23-Feb-2013
35.3	−92.72	2	3.38	85	70	−20	SLU	22-May-2013
35.57	−92.27	2	3.81	275	75	10	SLU	4-Jun-2014
36.05	−89.83	11	3.64	110	85	10	SLU	2-Apr-2015
42.21	−85.43	5	4.24	120	85	0	SLU	2-May-2015
38.46	−88.36	22	3.33	155	60	5	SLU	30-May-2015
35.66	−89.68	14	3.49	110	80	−5	SLU	25-Aug-2015
36.77	−90.85	17	3.48	125	85	20	SLU	16-Oct-2015

Note. The catalog acronyms are defined as the following: SLU is Saint Louis University Moment Tensor Catalog (Herrmann et al., 2011), GCMT is the Global-Centroid-Moment Tensor catalog (Ekström et al., 2010), and OIINK is the OIINK Catalog (Yang et al., 2014).

The computed orientations of maximum compressive stress across the study area take into account both the earthquake focal mechanisms, largely at depths greater than 4 km, and in situ stress indicators taken near the surface, predominantly in the upper 4 km (Lahann et al., 2017). We have no direct information on how the stress field varies with depth, so for simplicity, we assume that the shallow stress field, sampled by the various in situ observations, is similar to the stress field at greater depth sampled by the focal mechanism data. It has been shown that formal focal mechanism inversions, borehole breakouts, hydrofractures, overcores, and to a lesser extent core fracture and strain gauge measurements can provide information about regional stress orientations (e.g., Zoback, 2007; Zoback & Zoback, 1989, 1992). Additionally, Mazzotti and Townend (2010) show that maximum horizontal compressive stress orientations computed from focal mechanism data in the New Madrid Seismic Zone agree within 5–15° with borehole-derived maximum compressive stress orientations. Also, in Figure 1b, it is apparent that outside of the two seismic zones, S_{Hmax} orientations inferred from both data sets are fairly consistent with one another, suggesting that these measurements are more likely indicative of regional rather than local stresses (Figure 1c and section 4.2). Therefore, we believe that this simplification is acceptable as orientations derived from both in situ and earthquake focal mechanism data are likely similar and both representative of the stress field.

3. Methods

Inversion schemes for estimating the paleo-stress field from field measurements of fault striations and slickensides (e.g., Angelier, 1979, 1984, 1990; Angelier et al., 1982; Armijo et al., 1982; Carey & Brunier, 1974; Etchecopar et al., 1981; Michael, 1984; Reches, 1987) or the present-day state of stress from a population of focal mechanisms (e.g., Gephart & Forsyth, 1984; Gephart, 1990a, 1990b; Hardebeck & Michael, 2006; Michael, 1987a, 1987b, 1991) have been around for decades. The basis of these so-called stress inversions is the Wallace-Bott hypothesis that faults slip in the direction of maximum resolved shear stress (Bott, 1959; McKenzie, 1969; Wallace, 1951). From a collection of slip directions and fault orientations, a reduced stress tensor can be estimated. It is a reduced tensor in the sense that the full stress tensor cannot be uniquely determined from fault slip data, and therefore, a reduced stress state, described with fewer than six components, is estimated. The general technique in these stress inversions is to lump together a population of diverse focal mechanisms within a geographically restricted area that is assumed to be under a uniform state of stress and solve for the best fitting reduced stress tensor.

The mathematical relationship between stress tensor components and the direction of maximum shear stress on a fault (or direction of slip) is nonlinear. A number of different nonlinear inversion techniques have been adopted in the literature. Comparisons between different stress estimation algorithms show that the results from various methods are quite consistent (e.g., Balfour et al., 2005; Hardebeck & Hauksson, 2001a; Kastrup et al., 2004; Sherburn & White, 2005). However, as discussed by Arnold and Townend (2007), the estimated uncertainties in stress parameters can differ substantially (Balfour et al., 2005; Hardebeck & Hauksson, 2001b) and might be attributed to the different methods used to distinguish the nodal planes of each focal mechanism or the assumed error model. Arnold and Townend (2007) developed a Bayesian stress inversion to place robust estimates of uncertainties on estimated stress

Table 2
In Situ Maximum Horizontal Stress Orientation Data

Latitude (°N)	Longitude (°E)	Azimuth (°N E)	Data type	Ref
36.4	−82.92	71	Borehole breakout	World Stress Map (2015)
35.898	−90.034	73	Borehole breakout	World Stress Map (2015)
39.2	−81	85	Borehole breakout	World Stress Map (2015)
38.07	−89.92	76	Borehole breakout	World Stress Map (2015)
38	−88.95	99	Borehole breakout	World Stress Map (2015)
38.02	−89.21	119	Borehole breakout	World Stress Map (2015)
38.16	−89.17	72	Borehole breakout	World Stress Map (2015)
38.28	−88.35	50	Borehole breakout	World Stress Map (2015)
38.5	−88.65	73	Borehole breakout	World Stress Map (2015)
38.55	−87.7	88	Borehole breakout	World Stress Map (2015)
38.65	−88.3	56	Borehole breakout	World Stress Map (2015)
38.74	−87.78	89	Borehole breakout	World Stress Map (2015)
38.9	−87.8	65	Borehole breakout	World Stress Map (2015)
38.32	−87.46	96	Borehole breakout	World Stress Map (2015)
38.27	−87.73	85	Borehole breakout	World Stress Map (2015)
38.28	−87.82	101	Borehole breakout	World Stress Map (2015)
37.32	−87.5	99	Borehole breakout	World Stress Map (2015)
37.55	−87.82	91	Borehole breakout	World Stress Map (2015)
37.73	−87.42	94	Borehole breakout	World Stress Map (2015)
37.23	−83.15	51	Borehole breakout	World Stress Map (2015)
36.72	−83	55	Borehole breakout	World Stress Map (2015)
39.46	−82.44	58	Borehole breakout	World Stress Map (2015)
39.35	−82.04	60	Borehole breakout	World Stress Map (2015)
35.34	−91.82	75	Borehole breakout	World Stress Map (2015)
38.669	−86.885	125	Borehole breakout	IGWS PDMS
40.24	−85.172	75	Borehole breakout	IGWS PDMS
40.1	−85.475	80	Borehole breakout	IGWS PDMS
38.496	−89.662	73	Borehole breakout	New to Lahann et al. (2017)
38.003	−89.227	35	Borehole breakout	New to Lahann et al. (2017)
38.04	−88.993	102	Borehole breakout	New to Lahann et al. (2017)
38.635	−87.756	88	Borehole breakout	New to Lahann et al. (2017)
38.996	−87.863	72	Borehole breakout	New to Lahann et al. (2017)
38.133	−89.247	76	Borehole breakout	New to Lahann et al. (2017)
38.87	−82.13	75	Core fracture	World Stress Map (2015)
38.86	−81.88	60	Core fracture	World Stress Map (2015)
38.08	−82.16	65	Core fracture	World Stress Map (2015)
37.97	−83	65	Core fracture	World Stress Map (2015)
37.77	−82.42	63	Core fracture	World Stress Map (2015)
39.153	−89.433	62	Hydrofracture	New to Lahann et al. (2017)
41.861	−88.331	60	Hydrofracture	New to Lahann et al. (2017)
39.3	−89.35	62	Hydrofracture	World Stress Map (2015)
42.42	−89.9	48	Hydrofracture	World Stress Map (2015)
39.5	−82.5	64	Hydrofracture	World Stress Map (2015)
38.14	−82	60	Hydrofracture	World Stress Map (2015)
40.05	−82.53	62	Hydrofracture	World Stress Map (2015)
40.64	−83.92	70	Hydrofracture	World Stress Map (2015)
38	−81.4	64	Overcoring	World Stress Map (2015)
39.515	−89.509	73	Overcoring	New to Lahann et al. (2017)
41.77	−87.854	72	Overcoring	New to Lahann et al. (2017)
38.404	−87.806	101	Overcoring	New to Lahann et al. (2017)
38.346	−87.872	85	Overcoring	New to Lahann et al. (2017)
37.891	−88.551	78	Overcoring	New to Lahann et al. (2017)
39.189	−89.885	57	Overcoring	New to Lahann et al. (2017)
37.918	−88.817	76	Strain gauge	New to Lahann et al. (2017)
37.984	−88.941	112	Strain gauge	New to Lahann et al. (2017)
39.134	−88.889	70	Strain gauge	New to Lahann et al. (2017)
41.835	−87.869	75	Strain gauge	New to Lahann et al. (2017)
36.12	−89.67	82	Stress inversion	Mazzotti and Townend (2010)

Note. All sources cited in the table and in the references. IGWS PDMS refers to the Indiana Geological and Water Survey Petroleum Database Management System. Where quality rankings are provided, only A–C rankings were used.

components. This method accounts for uncertainties in the focal mechanism parameters and the nodal plane ambiguity. Vavryčuk (2014) selected the nodal plane that is nearest to optimal orientation according to Mohr-Coulomb friction.

While many inversion methods solve for a single stress tensor from a population of earthquake focal mechanisms, Hardebeck and Michael (2006) use the linearized formulation of Michael (1984) to solve for a spatially varying stress state, assuming that the stress field varies smoothly in space (damped least squares). The advantage of this method is that one does not have to decide a priori, or as part of the inversion algorithm, which subsets of the entire focal mechanism population can be attributed to a single stress tensor. Although an estimate of the uncertainties in the individual estimated stress tensor components by propagation of errors in the Hardebeck and Michael (2006) inversion could be determined, the focal mechanism errors are unknown and the uncertainty in selection of the nodal plane is not considered. The Arnold and Townend (2007) method is designed precisely to remedy this problem. However, it is a computationally expensive method to estimate the reduced stress tensor components on a large number of points in space connected through a spatial smoothing prior as in Hardebeck and Michael (2006). In this paper, we build on the methods outlined above to construct an inversion of spatially heterogeneous focal mechanisms for the 2-D or 3-D spatial distribution of the reduced stress tensor. The method is designed to efficiently combine the relative strengths of Hardebeck and Michael (2006) damped linear least squares inversion and the Arnold and Townend (2007) nonlinear Bayesian inversion. We combine aspects of these two approaches with the mixed linear/nonlinear Bayesian inversion scheme of Fukuda and Johnson (2010). Yang et al. (2013) used a similar Bayesian method for objectively determining spatial smoothing in an inversion for absolute deviatoric stress state in northern Japan, but did not incorporate nodal plane selection.

3.1. Linear Inversion

Michael (1984) proposed a linearized stress inversion for a normalized deviatoric stress state using a set of focal mechanisms. Hardebeck and Michael (2006) extended the Michael (1984) method to invert for a spatially varying stress field as a damped least squares inversion. For a fault plane with normal vector, $\mathbf{n} = [n_1, n_2, n_3]^T$, the shear traction vector, $\boldsymbol{\tau}$, on the fault under stress tensor, $\boldsymbol{\sigma}$, is

$$\boldsymbol{\tau} = \boldsymbol{\sigma}\mathbf{n} - [(\boldsymbol{\sigma}\mathbf{n})\cdot\mathbf{n}]\mathbf{n}. \tag{1}$$

Michael (1984) assumed that the fault slips in the direction of maximum shear stress on the fault. In this case, the unit slip vector, $\mathbf{s}$, can be written

$$\mathbf{s} = \frac{\boldsymbol{\tau}}{|\boldsymbol{\tau}|} \tag{2}$$

where $|\boldsymbol{\tau}|$ is the magnitude of shear stress. Equations (1) and (2) together give a linear relationship between the components of the unit slip vector, $\mathbf{s}$, and the stress tensor, $\boldsymbol{\sigma}$, normalized by the magnitude of the shear stress. In order to establish a linear relationship between the components of the stress tensor and the components of the unit slip vector, Michael (1984) assumed that the magnitude of the shear stress, $|\boldsymbol{\tau}|$, is the same on all faults, regardless of orientation. Although this is seemingly a poor assumption, given that magnitude of the shear stress is of course dependent on orientation of the plane relative to the principal stress directions, the method has been accepted because it has been demonstrated to give reasonable results. Because the orientation of maximum shear stress on a surface is insensitive to mean stress, Michael (1984) assumed, for simplicity, $\sigma_{33} = -(\sigma_{11} + \sigma_{22})$.

We divide the region containing focal mechanisms into a number of volume cells and invert for the stress tensor in each cell with the condition that the stress tensor components vary smoothly from one cell to a neighboring cell. Following the notation of Hardebeck and Michael (2006), a 5×1 vector of stress tensor components, $\sigma_i = [\sigma^i_{11}, \sigma^i_{12}, \sigma^i_{13}, \sigma^i_{22}, \sigma^i_{23}]^T$ in the ith cell containing k focal mechanisms are related to the jth fault plane normal $[n_{j1}, n_{j2}, n_{j3}]^T$ and jth unit slip vector, $\mathbf{s}_j = [s_{j1}, s_{j2}, s_{j3}]^T$, j = 1, 2, ..., k, through the linearized relationship of Michael (1984),

$$\mathbf{s_i} = \mathbf{G_i}\boldsymbol{\sigma_i} + \boldsymbol{\epsilon} \tag{3}$$

where $\boldsymbol{\epsilon}$ is a vector of errors and the data kernel matrix is

$$\mathbf{G_i} = \begin{pmatrix} n_{11} - n_{11}^3 + n_{11}n_{13}^2 & n_{12} - 2n_{11}^2 n_{12} & n_{13} - 2_{n11}^2 n_{13} & n_{11}n_{13}^2 - n_{11}n_{12}^2 & -2n_{11}n_{12}n_{13} \\ n_{12}n_{13}^2 - n_{12}n_{11}^2 & n_{11} - 2n_{12}^2 n_{11} & -2n_{11}n_{12}n_{13} & n_{12} - n_{12}^3 + n_{12}n_{13}^2 & n_{13} - 2n_{12}^2 n_{13} \\ n_{13}^3 - n_{13}n_{11}^2 - n_{13} & -2n_{11}n_{12}n_{13} & n_{11} - 2n_{13}^2 n_{11} & n_{13}^3 - n_{13}n_{12}^2 - n_{13} & n_{12} - 2n_{13}^2 n_{12} \\ \vdots & \vdots & \vdots & \vdots & \vdots \\ n_{k1} - n_{k1}^3 + n_{k1}n_{k3}^2 & n_{k2} - 2n_{k1}^2 n_{k2} & n_{k3} - 2n_{k1}^2 n_{k3} & n_{k1}n_{k3}^2 - n_{k1}n_{k2}^2 & -2n_{k1}n_{k2}n_{k3} \\ n_{k2}n_{k3}^2 - n_{k2}n_{k1}^2 & n_{k1} - 2n_{k2}^2 n_{k1} & -2n_{k1}n_{k2}n_{k3} & n_{k2} - n_{k2}^3 + n_{k2}n_{k3}^2 & n_{k3} - 2n_{k2}^2 n_{k3} \\ n_{k3}^3 - n_{k3}n_{k1}^2 - n_{k3} & -2n_{k1}n_{k2}n_{k3} & n_{k1} - 2n_{k3}n_{k1} & n_{k3}^3 - n_{k3}n_{k2}^2 - n_{k3} & n_{k2} - 2n_{k3}^2 n_{k2} \end{pmatrix} \quad (4)$$

For M cells,

$$\begin{pmatrix} \boldsymbol{s_1} \\ \boldsymbol{s_2} \\ \vdots \\ \boldsymbol{s}_M \end{pmatrix} = \begin{pmatrix} G_1 & 0 & \dots & 0 \\ 0 & G_2 & \dots & 0 \\ 0 & 0 & \ddots & 0 \\ 0 & 0 & 0 & G_M \end{pmatrix} \begin{pmatrix} \boldsymbol{\sigma}_1 \\ \boldsymbol{\sigma}_2 \\ \vdots \\ \boldsymbol{\sigma}_M \end{pmatrix} + \epsilon. \quad (5)$$

We rewrite equation (5) as $\boldsymbol{s} = \boldsymbol{G\sigma} + \boldsymbol{\epsilon}$ and assume Gaussian errors for the focal mechanism data, $\boldsymbol{\epsilon} \sim N(0, \sigma_d{}^2 \boldsymbol{I})$, where $\boldsymbol{I}$ is the identity matrix and $\sigma_d{}^2$ is the data variance. Hardebeck and Michael (2006) solve a damped least squares inversion for stress by minimizing a combination of sum of squared residuals and the length of first-derivative smoothing vector,

$$\Phi = \sigma_d{}^{-2} \|\mathbf{s} - \mathbf{G\sigma}\|^2 + \beta^{-2} \|\mathbf{D\sigma}\|^2 \quad (6)$$

where $\| \ \|$ denotes L2 norm and $\mathbf{D}$ is the first-derivative smoothing operator. The smoothing parameter, β^2, provides the relative weighting placed on minimizing the misfit between predicted and observed slip vectors (first term on right-hand side) and the norm of model roughness (second term on right-hand side). Hardebeck and Michael (2006) select the smoothing parameter from a trade-off curve.

3.2. Incorporating In Situ Data

To incorporate in situ data, we have to augment this system of equations (5). We recognize that the horizontal component of the resolved shear traction on planes with strike parallel to S_{Hmax} is zero. Let α be the orientation of S_{Hmax} relative to the x_1 direction (Figure 2). Then the horizontal component of the shear traction, τ, on any plane with strike parallel to S_{Hmax} is

$$\tau = 0 = \frac{\sigma_{11} - \sigma_{22}}{2} \sin 2\alpha + \sigma_{12} \cos 2\alpha. \quad (7)$$

Thus, for the ith cell containing k S_{Hmax} orientations, we can write

$$\mathbf{0} = \mathbf{H_i \sigma_i} \quad (8)$$

where

$$\mathbf{H_i} = \begin{pmatrix} \frac{1}{2}\sin 2\alpha_1 & \cos 2\alpha_1 & 0 & -\frac{1}{2}\sin 2\alpha_1 & 0 \\ \frac{1}{2}\sin 2\alpha_2 & \cos 2\alpha_2 & 0 & -\frac{1}{2}\sin 2\alpha_2 & 0 \\ \vdots & \vdots & \vdots & \vdots & \vdots \\ \frac{1}{2}\sin 2\alpha_k & \cos 2\alpha_k & 0 & -\frac{1}{2}\sin 2\alpha_k & 0 \end{pmatrix}. \quad (9)$$

Equation (8) does not alone constrain the S_{Hmax} orientation because a stress state with S_{Hmax} oriented at angle $\alpha + 90^\circ$ also satisfies these equations. That is, the equations only state that either S_{Hmax} or S_{hmin}

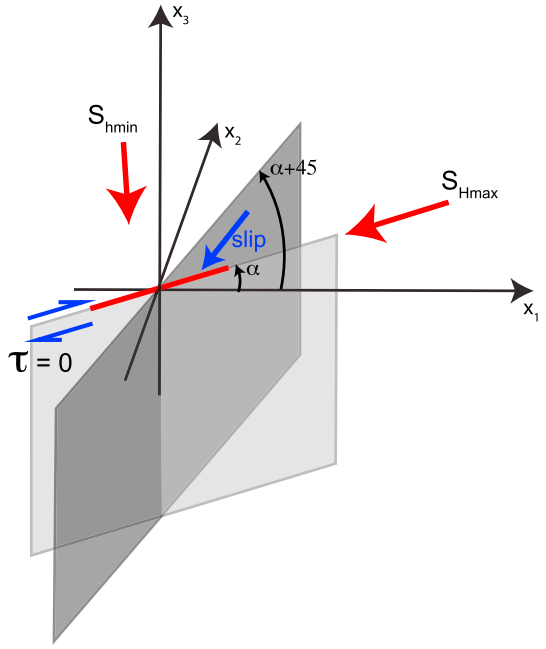

Figure 2. Illustration of constraints on stress from S_{Hmax} orientation. Shear stress is zero on any plane containing S_{Hmax}, oriented at angle α to the x_1 direction (here shown as a vertical plane). Also shown is sense of horizontal component of slip on plane oriented α + 45° to the x_1 direction.

has orientation of α. To remove this ambiguity and constrain S_{Hmax} to the α orientation, we note that sense of horizontal slip on a vertical plane with strike $\alpha + 45^{\circ}$ will be right-lateral sense only if α is the S_{Hmax} orientation. Thus, we add the further constraint that the horizontal component of slip, $[s_1, s_2, 0]^T$ on this plane is in the direction $[\cos(\alpha+\frac{\pi}{4}), \sin(\alpha+\frac{\pi}{4}), 0]^T$. Again, considering the ith cell containing k S_{Hmax} orientations,

$$\mathbf{s^H_i}=\mathbf{K_i}\boldsymbol{\sigma}_\mathbf{i} \tag{10}$$

where $\mathbf{s_i^H}$ is a $2\,k\times1$ vector of horizontal slip vectors,

$$\mathbf{s^H_i}=\begin{pmatrix}\cos\left(\alpha_1+\frac{\pi}{4}\right)\\ \sin\left(\alpha_1+\frac{\pi}{4}\right)\\ \vdots\\ \sin\left(\alpha_k+\frac{\pi}{4}\right)\\ \sin\left(\alpha_k+\frac{\pi}{4}\right)\end{pmatrix} \tag{11}$$

and

$$\mathbf{K_i}=\begin{pmatrix} n_{11}-n_{11}^3+n_{11}n_{13}^2 & n_{12}-2n_{11}^2n_{12} & n_{13}-2_{n11}^2n_{13} & n_{11}n_{13}^2-n_{11}n_{12}^2 & -2n_{11}n_{12}n_{13}\\ n_{12}n_{13}^2-n_{12}n_{11}^2 & n_{11}-2n_{12}^2n_{11} & -2n_{11}n_{12}n_{13} & n_{12}-n_{12}^3+n_{12}n_{13}^2 & n_{13}-2n_{13}n_{12}^2\\ \vdots & \vdots & \vdots & \vdots & \vdots\\ n_{k1}-n_{k1}^3+n_{k1}n_{k3}^2 & n_{k2}-2n_{k1}^2n_{k2} & n_{k3}-2n_{k1}^2n_{k3} & n_{k1}n_{k3}^2-n_{k1}n_{k2}^2 & -2n_{k1}n_{k2}n_{k3}\end{pmatrix} \tag{12}$$

where the normal vectors to the planes are

$$\begin{pmatrix} n_{i1}\\ n_{i2}\\ n_{i3}\end{pmatrix}=\begin{pmatrix}\sin\left(\alpha_i+\frac{\pi}{4}\right)\\ -\cos\left(\alpha_i+\frac{\pi}{4}\right)\\ 0\end{pmatrix}. \tag{13}$$

Combining the focal mechanism and in situ constraints in the ith cell, and introducing variances on focal mechanism slip vector components, σ_{fm}^2, and in situ orientations, σ_{SH}^2, we can form the weighted system of equations

$$\begin{pmatrix}\frac{1}{\sigma_{fm}}\mathbf{s_i}\\ \mathbf{0}\\ \frac{1}{\sigma_{SH}}\mathbf{s^H_i}\end{pmatrix}=\begin{pmatrix}\frac{1}{\sigma_{fm}}\mathbf{G_i}\\ \frac{1}{\sigma_{SH}}\mathbf{H_i}\\ \frac{1}{\sigma_{SH}}\mathbf{K_i}\end{pmatrix}\boldsymbol{\sigma}_\mathbf{i}. \tag{14}$$

Writing this augmented system of weighted equations as

$$\mathbf{s^*_i}=\mathbf{G^*_i}\boldsymbol{\sigma}_\mathbf{i} \tag{15}$$

for M cells, we have the large, sparse, system of equations

$$\begin{pmatrix} \mathbf{s}^*_1 \\ \mathbf{s}^*_2 \\ \vdots \\ \mathbf{s}^*_M \end{pmatrix} = \begin{pmatrix} G^*_1 & 0 & \dots & 0 \\ 0 & G^*_2 & \dots & 0 \\ 0 & 0 & \ddots & 0 \\ 0 & 0 & 0 & G^*_M \end{pmatrix} \begin{pmatrix} \boldsymbol{\sigma}_1 \\ \boldsymbol{\sigma}_2 \\ \vdots \\ \boldsymbol{\sigma}_M \end{pmatrix}. \tag{16}$$

3.3. Bayesian Inversion of Linear and Nonlinear Parameters

We also introduce binary parameters $P_1, P_2, \dots, P_K$ for the K focal mechanisms. The P_i have a value of either 1 or 2 to represent either the first or second nodal plane. To simplify notation, let $\Sigma = [\sigma_1, \sigma_2, \dots, \sigma_N]^T$ be the vector of all unknown stress tensor components, let $P = [P_1, P_2, \dots, P_K]^T$ be the vector of all binary parameters, and let $\mathbf{s} = [\mathbf{s}^*_1, \mathbf{s}^*_2, \dots, \mathbf{s}^*_M]^T$. Let β^2 be the smoothing parameter for first-derivative spatial smoothing (as introduced in equation (6)). We assume that the data variances,σ^2_{fm} and σ^2_{SH}, are unknown. The solution to this inverse problem is the joint posterior probability density function (PDF) of unknown parameters given $\mathbf{s}$,

$$p\left(\Sigma, P, \sigma^2_{fm}, \sigma^2_{SH}, \beta^2 | \mathbf{s}\right). \tag{17}$$

The stress tensor components are related linearly to the data (equation (15)), while the other parameters are nonlinearly related to the observations. This is therefore a mixed linear-nonlinear inversion. We adopt the methodology of Fukuda and Johnson (2010) that combines both linear least squares methods and Monte Carlo methods to estimate the PDF (17).

As discussed in Fukuda and Johnson (2010), the linear and nonlinear parameter in the PDF (17) can be separated (by identity) as

$$p\left(\Sigma, P, \sigma^2_{fm}, \sigma^2_{SH}, \beta^2 | \mathbf{s}\right) = p\left(\Sigma | \mathbf{s}, P, \sigma^2_{fm}, \sigma^2_{SH}, \beta^2\right) p\left(P, \sigma^2_{fm}, \sigma^2_{SH}, \beta^2 | \mathbf{s}\right). \tag{18}$$

The mean and standard deviation of the Gaussian distribution, $p(\Sigma|\,\mathbf{s}, P, \sigma^2_{fm}, \sigma^2_{SH}, \beta^2)$, are computed using linear least squares formulas, and the non-Gaussian PDF $p(P, \sigma^2_{fm}, \sigma^2_{SH}, \beta^2|\,\mathbf{s})$ is evalutated using Monte Carlo Markov chain (MCMC) methods. According to Baye's theorem, the posterior PDF of the linear parameters can be written with the proportionality

$$p\left(\Sigma\,|\mathbf{s}, P, \sigma^2_{fm}, \sigma^2_{SH}, \beta^2\right) \propto p\left(\mathbf{s}|\Sigma, P, \sigma^2_{fm}, \sigma^2_{SH}\right) p\left(\Sigma|\beta^2\right) \tag{19}$$

where $p(\mathbf{s}|\,\Sigma, P, \sigma^2_{fm}, \sigma^2_{SH})$ is likelihood and $p(\Sigma|\,\beta^2)$ is the prior distribution on stress tensor components assuming no prior information on the other parameters. Here we assume the prior distribution

$$p\left(\Sigma|\beta^2\right) = \left(2\pi\beta^2\right)^{-5M/2} \exp\left[-\frac{1}{2\beta^2}(\mathbf{D}\Sigma)^T(\mathbf{D}\Sigma)\right] \tag{20}$$

where $\mathbf{D}$ is the first-derivative operator. This prior is a statement that the spatial derivative of stress components is zero with variance β^2. We have assumed Gaussian errors for the observed slip vector components and S_{Hmax} directions, so the likelihood is

$$p\left(\mathbf{s}\middle|\Sigma, P, \sigma^2_{fm}, \sigma^2_{SH}\right) = \left(2\pi{\sigma_{fm}}^2\right)^{-N_{fm}/2} \left(2\pi{\sigma_{SH}}^2\right)^{-N_{SH}/2} \exp\left[-\frac{1}{2}(\mathbf{s} - \mathbf{G}(\mathbf{P})\Sigma)^T(\mathbf{s} - \mathbf{G}(\mathbf{P})\Sigma)\right] \tag{21}$$

where $\mathbf{G}$ here is the augmented weighted kernel matrix in equation (16) and is a function of the selected nodal plane, P. N_{fm} and N_{SH} are the number of focal mechanisms and in situ data, respectively. Fukuda and Johnson (2010) provide details about how to compute the target posterior PDF (17) by combining linear least squares and MCMC methodologies. In Appendix A, we illustrate and validate this inversion method for a 2-D stress state and synthetic focal mechanism data.

3.4. Cell Size

We determined the optimal number of volume cells for our inversions empirically. We conducted a suite of stress inversions in which we held smoothing and standard deviation parameters constant while varying only the grid cell size. Our criteria were that the grid must be just fine enough to capture spatial heterogeneities in S_{Hmax} orientations with small ($<30°$) misfit angles between observed slip and computed shear stress directions. We found that cell size does not exert a major control over the resultant stress field after a certain

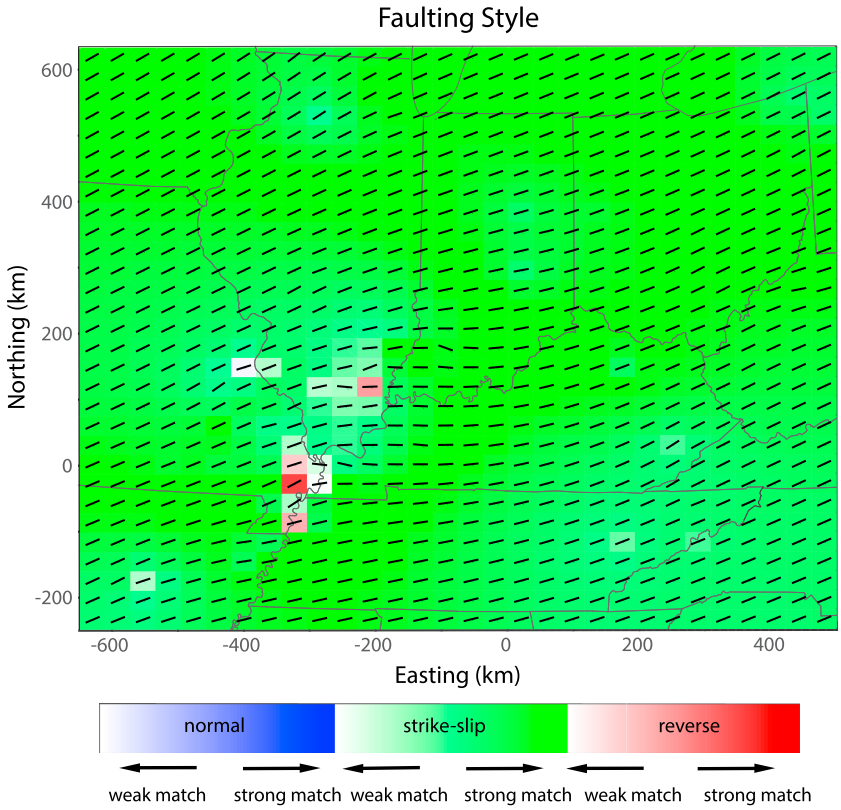

Figure 3. Maximum horizontal stress directions and dominant faulting styles determined using both the focal mechanism and in situ data. The red shows reverse faulting, the green shows strike slip, and the blue shows normal faulting. Depth of the color shows agreement with Anderson's definition of faulting, the darker color indicates a stronger match, or closer to the pure definition of faulting with one vertical and two horizontal stresses.

level of grid fineness is reached. The grid size we chose to best represent the stress field is a 30 × 30 grid with cell dimensions of approximately 38 km × 29 km.

4. Results

4.1. Markov Chain Monte Carlo Joint Inversion

The results of the stress inversion showing faulting style and orientation of maximum horizontal stress are shown in Figure 3. Coloring depicts dominant style of faulting with red representing reverse faulting, green strike-slip faulting, and blue normal faulting. Following the definition of Anderson (1905, 1951), faulting style is determined through orientation of the principal stresses (σ_1, σ_2, and σ_3). In Figure 3, the depth of the color depends on the degree between 0 (dark) and 45 (white) to which the nearest to vertical stress deviates from the vertical direction (e.g., Yang et al., 2013). A pure strike-slip or dip-slip faulting style will have one of the three principal stresses exactly in the vertical direction (a "strong match") and will show the darkest color. A faulting style where the resultant principal stress orientations are not vertical and horizontal shows a lighter color (a "weak match") and represents a faulting regime in which multiple faulting styles are present or oblique faulting earthquakes dominate. The orientations of maximum horizontal stress are shown as black tick marks. In areas where the faulting style is purely strike-slip or reverse, the direction of maximum horizontal stress is the maximum principal stress.

The inversion results show a relatively homogenous stress field across the study area, varying between N60°E and N80°E, but locally can vary as much as ~E/W to N70°W/S70°E. The stress regime is nearly uniformly strike slip (vertical intermediate compressive stress) across the study area, which is unsurprising given that the region is dominated by strike-slip focal mechanisms. Both the New Madrid and Wabash Valley Seismic Zones show a transition to a reverse faulting stress regime (vertical minimum compressive stress) over rather short spatial scales (within ~40–120 km). This could occur if the intermediate and minimum principal stresses

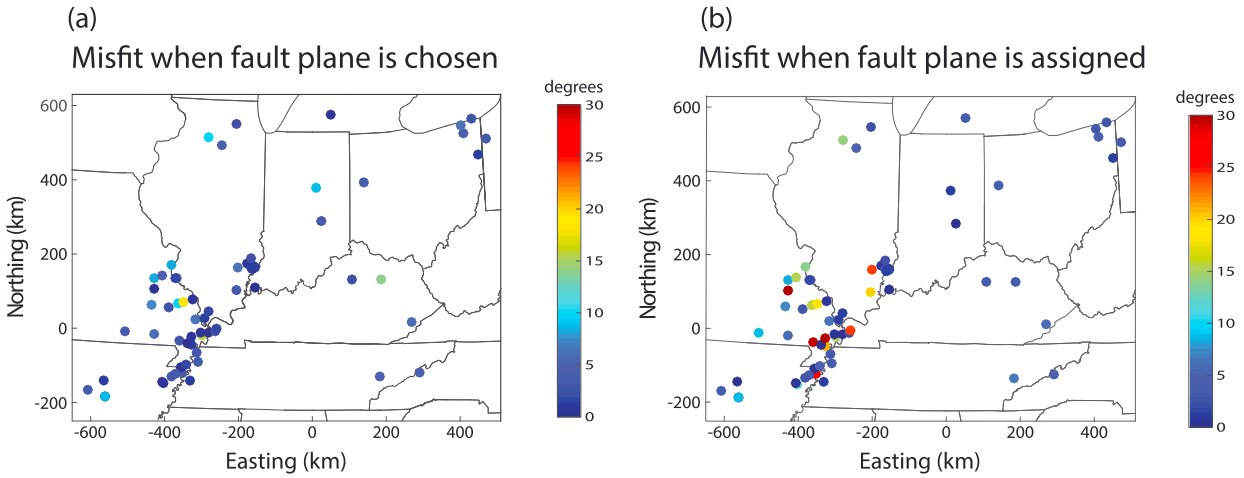

Figure 4. (a) Misfit angles where the best fitting nodal plane is chosen as the fault plane. Misfit angles are all below 20°, showing very good fit. (b) Misfit angles where plane 1 is assigned as the fault plane.

are nearly equal in magnitude ($S_V \approx S_{hmin}$), as suggested for this region by Hurd and Zoback (2012a). This anomalous zone of increased compression is located in the northern New Madrid Seismic Zone and Wabash Valley Seismic Zone, while the remainder of the study area maintains a pure strike-slip stress regime ($S_{Hmax} > S_V > S_{hmin}$).

Misfit angles between the computed direction of maximum shear stress and observed slip directions from the focal mechanisms are all less than 20°, with most less than 5° (Figure 4a). Uncertainties in focal mechanism orientations are typically less than 20° and often as low as 5° (e.g., Hardebeck & Hauksson, 2001b). We do not have formal uncertainties on the focal mechanism orientation data; however, because the misfit angles are similar to typical reported uncertainties in focal mechanism orientations, this suggests that the inversion is not overfitting or underfitting the data.

The low misfit angles are partially a consequence of the MCMC selection of the optimally fitting nodal plane. A comparison of the misfit angles for the inversion with fault plane selection and an inversion with fixed fault plane is shown in Figures 4a and 4b, respectively. Although both show misfit angles typically lower than 30°, it is clear for many mechanisms that one of the nodal planes fits significantly better than the alternate nodal

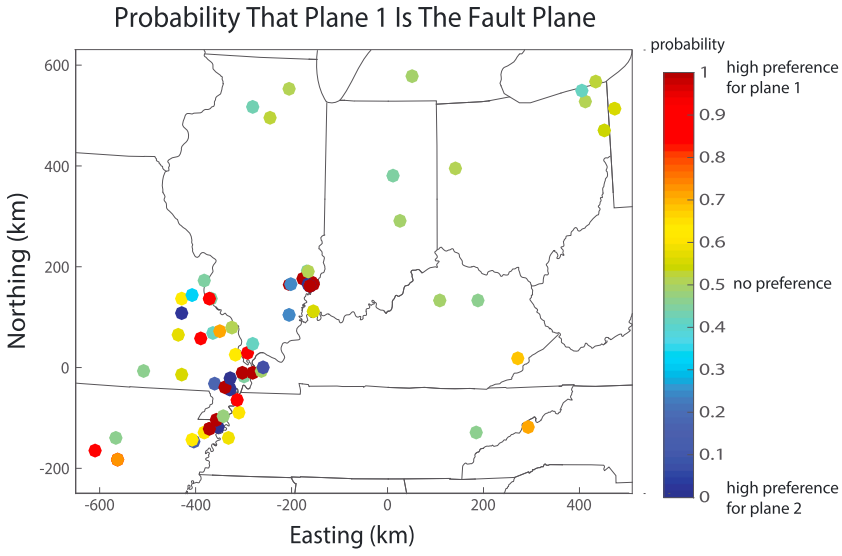

Figure 5. Probability that nodal plane 1 is the fault plane. Probabilities near 0.5 indicate that the inversion finds no preference for fault plane. Probabilities near one indicate preference for plane 1, and probabilities near zero indicate preference for plane 2.

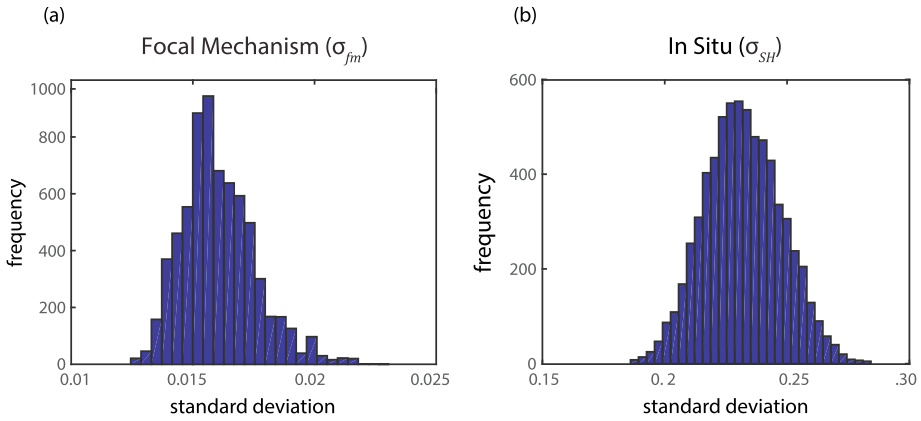

Figure 6. Histograms of standard deviation values from the objectively determined data variances, which show relative weighting of the two data sets. (a) Histogram of focal mechanism standard deviation. (b) Histogram of in situ standard deviation.

plane. For some of the mechanisms, the misfit is reduced by up to 25° when the fault plane is not arbitrarily fixed, substantially improving the fit to the focal mechanism data. Figure 5 quantifies this by plotting the probability that the first nodal plane, which is an arbitrary designation, is selected as the fault plane. The red indicates that the first nodal plane is highly preferred, the blue indicates that the second nodal plane is highly preferred, and the green indicates no preference. Many mechanisms show strong nodal plane preference, largely concentrated near the Midcontinent Seismic Zones.

The relative weighting of the two data sets is expressed as data variances (as introduced in equation (17)). Figure 6 shows histograms of standard deviation values (the square root of the data variances) for the two data sets, which are objectively determined in the inversion. The standard deviation value for the focal mechanism solutions is $\sigma_{fm} = 0.016$, an order of magnitude smaller than the in situ orientations, which have a value of $\sigma_{SH} = 0.230$. The focal mechanism solutions are weighted more heavily in the inversion than the in situ data because they have a smaller standard deviation (and variance) value.

Angular uncertainties for the computed S_{Hmax} orientations derived from the inversion are shown in Figure 7a, with 95% confidence limits denoted by the circular wedges centered on the mean derived S_{Hmax} orientation. Figure 7b shows the 95% confidence range in degrees. Regions with little or no data, such as the corners of the study area, show higher uncertainties. Regions where data density is high show smaller uncertainties.

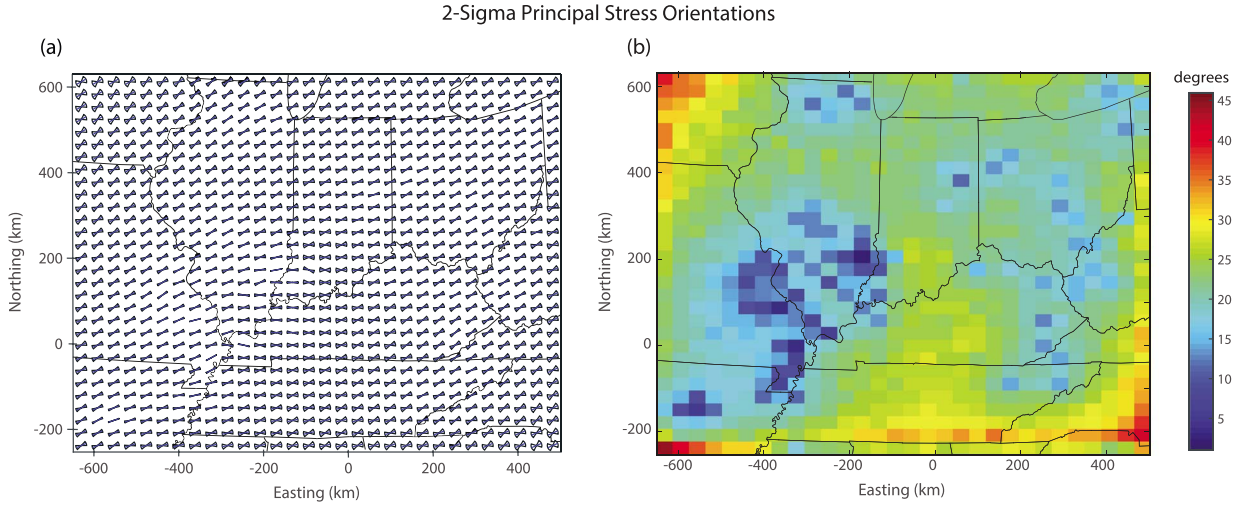

Figure 7. (a) 2-sigma uncertainties in maximum compressive stress orientations displayed as semicircles with mean maximum horizontal stress orientation in the center. (b) 2-sigma standard deviation in degrees from orientation of maximum compressive stress.

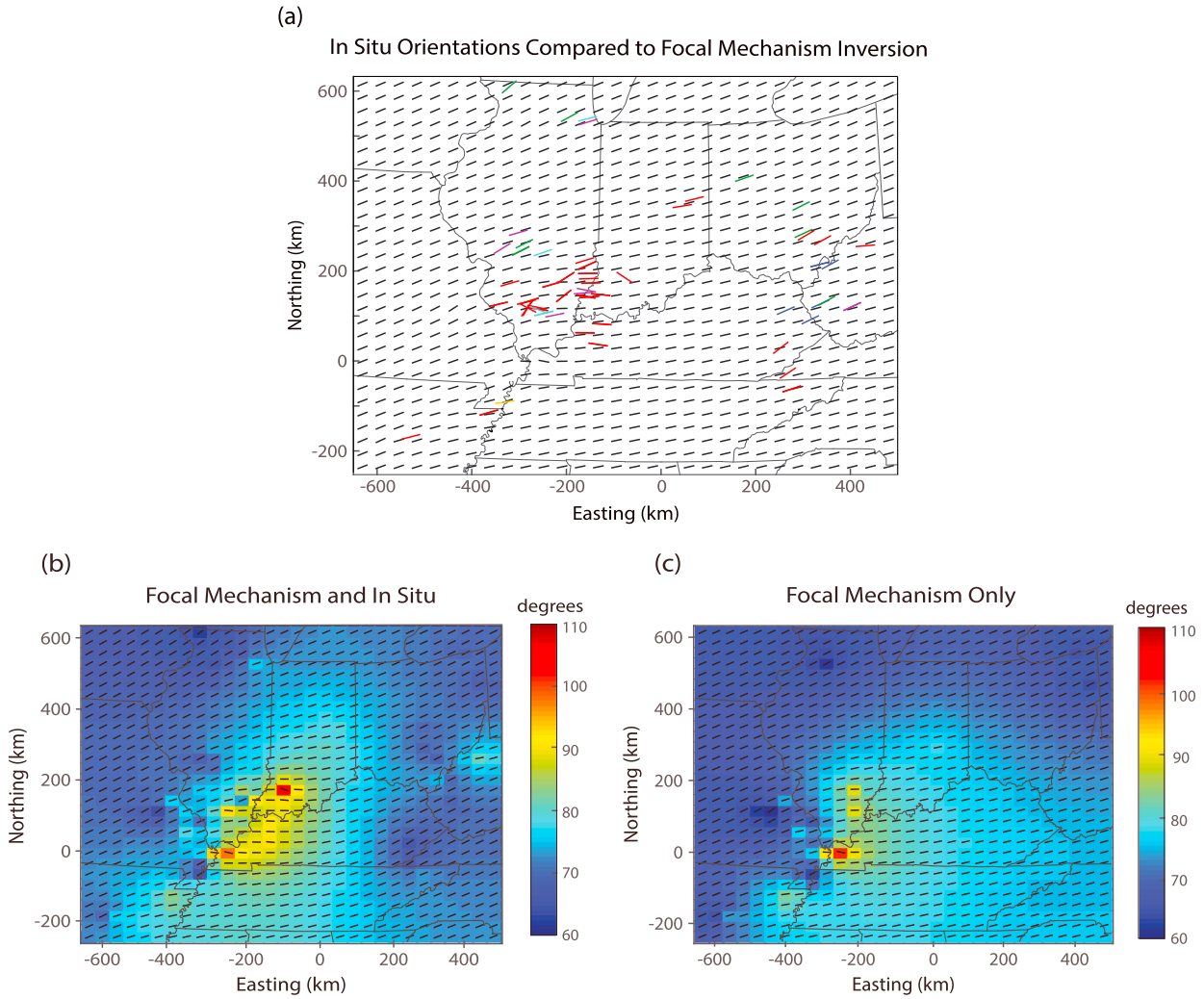

Figure 8. (a) Comparison of computed maximum horizontal stress orientations using only focal mechanism data with in situ orientations (colors as in Figure 1c). (b) Orientation of maximum horizontal stress orientations in degrees derived from inversion of focal mechanism and in situ data. (c) Orientation of maximum horizontal stress orientations in degrees derived from focal mechanism data only.

4.2. Comparison of Focal Mechanism Only Inversion to Combined Inversion

To examine the degree to which the estimated principal stress orientations are controlled by the two different data sets, we conducted an inversion using only focal mechanism solutions. This solution compared to the in situ orientations and the inversion that combines both data sets is shown in Figure 8. Figure 8a shows the computed S_{Hmax} orientations using an inversion of only the focal mechanism data overlain by in situ observations. While the general pattern of the inverted S_{Hmax} orientations agrees with most of the observations, there are systematic differences of up to about 20° near the tristate region of Indiana, Illinois, and Kentucky (−200 km east, 100 km north) and also in portions of eastern Kentucky and western West Virginia (300 km east, 100 km north).

Figures 8b and 8c show the azimuth of maximum horizontal stress orientations for the two inversions. Comparing the orientations of maximum horizontal stress derived using both the focal mechanism data and the in situ data (Figure 8b) with the inversion using only the focal mechanism data (Figure 8c) reveals where in the study area the in situ data most influences the determination of the stress field. Deviation from the dominant N60°E–N70°E orientation is slightly higher and covers a broader area in the inversion with both data sets than in the focal mechanism-only inversion, particularly in southern Indiana and western Kentucky where the majority of the in situ orientations are found. Additionally, in the focal mechanism-only inversion,

N75°E–N80°E is the dominant orientation across the entire eastern section of the study area. In the inversion that considers both data sets, the maximum horizontal stress orientation is N60°E–N70°E in the area further to the east. After incorporating the in situ orientations, we can see that the nearly E-W rotation in maximum compressive stress is highly concentrated in the Wabash Valley and northern New Madrid Seismic Zones. The additional data, especially in the eastern half of the study area where there are fewer focal mechanisms, better constrain the region where the rotation in the stress field occurs.

The largest rotation in maximum compressive stress is an ~N70°W orientation located in southern Indiana (−80 km east, 180 km north). Due to poor data coverage in this region, we suspect that the orientation may be controlled by a single borehole breakout located in southern Indiana (38.669 latitude, −86.885 longitude) with an azimuth of 125°. To test this, we removed this in situ orientation and conducted the same inversion as before. Removing this data point did alter the orientation of maximum horizontal stress in the cell containing the borehole breakout measurement, but only slightly modifies the regional stress distribution. This result can be found in Figure S1.

5. Discussion

Across the Midcontinent, the maximum horizontal stress is oriented between N60°E and N80°E, as summarized in Figure 9. The average regional trend of S_{Hmax} is ~N60°E–N70°E; however, there is a systematic rotation of S_{Hmax} to ~E-W in the southern Illinois Basin, northern New Madrid Seismic Zone, Wabash Valley Seismic Zone, and in the vicinity of the Rough Creek Graben in western Kentucky (Figure 9). The largest deviation from the regional trend is a N70°W S_{Hmax} orientation located in southwestern Indiana; however, this may be controlled by a single borehole breakout measurement.

Areas of reverse faulting stress regime occur in the New Madrid and Wabash Valley Seismic Zones. Although absolute magnitudes of the principal stresses cannot be determined using this stress inversion, we can use this information to speculate about the relative magnitudes of the principal stresses. The transition from strike-slip to reverse faulting stress regime in the New Madrid and Wabash Valley regions shows that the vertical stress alternates between the intermediate and minimum principal stresses, indicating that the vertical stress and the minimum horizontal stress are likely similar in magnitude. This relationship appears to be highly concentrated in this zone. Outside of the northern New Madrid and Wabash Valley Seismic Zones, the faulting style is purely strike slip, indicating that the vertical stress is greater than the minimum horizontal stress. Relative magnitudes of the principal stresses are used to describe the faulting regime and are often expressed using the A_ϕ parameter (Simpson, 1997). A plot showing the spatially varying A_ϕ parameter is included in Figure S2.

Reactivation of faults associated with the Rough Creek Graben, adjacent to and of similar age as the Reelfoot Rift in western Kentucky has not been observed. Faults in this zone are steeply dipping, graben-bounding normal faults generally striking E-W (Soderberg & Keller, 1981). Although there are only two in situ stress orientation measurements in the vicinity of the Rough Creek Graben (latitude 37.32, longitude −87.5 and latitude 37.55, longitude −87.82) and no focal mechanisms, the smoothed nature of the stress inversion allows us to interpolate across cells lacking data. In western Kentucky, where the strike of the faults associated with the Rough Creek Graben are ~E-W, S_{Hmax} is oriented approximately parallel to the strike of faults, implying low resolved shear stress on faults, which is consistent with the lack of observed seismicity. Although data density is low and there may be other reasons for the lack of observed seismicity near the Rough Creek Graben (different frictional or structural properties, for example), the agreement between fault orientation and S_{Hmax} orientation with a lack of seismicity in this region provides additional support for our interpolated S_{Hmax} orientations.

Similar failed rift systems exist in the United States, and undoubtedly, many faults in the region are optimally oriented to the direction of maximum compressive stress; however, few produce seismic events at the same rate or magnitude as the closely spaced New Madrid, Wabash Valley, and St. Genevieve Seismic Zones. There are many theories as to why we have large-magnitude events and high rates of seismicity in the Midcontinent, including a weak zone in the lower crust and upper mantle causing stresses to concentrate (Chen et al., 2016; Kenner & Segall, 2000; Pollitz & Mooney, 2013), glacial isostatic readjustment (Grollimund & Zoback, 2001), unloading due to increased Holocene erosion rates in the Mississippi River

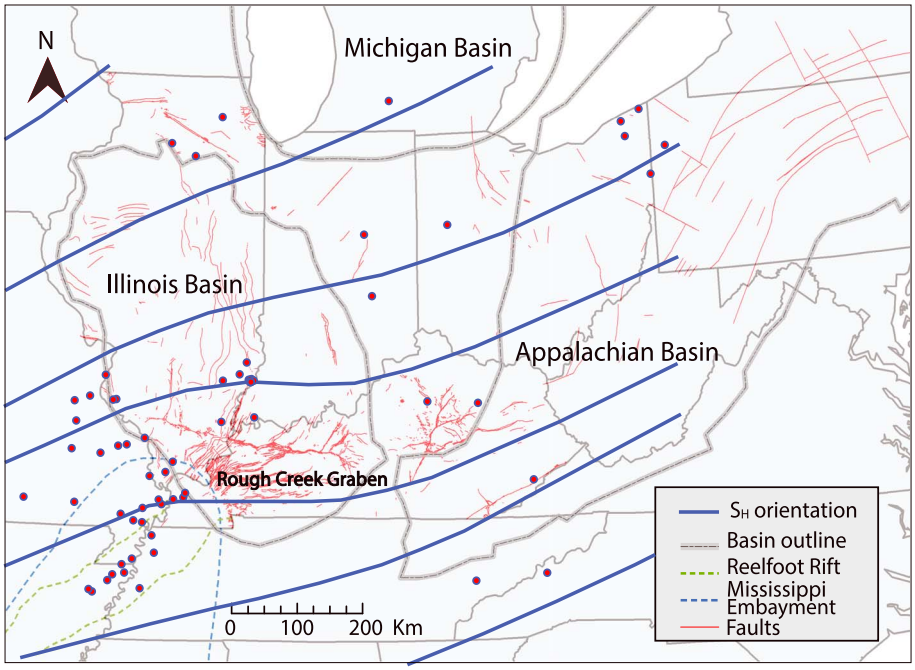

Figure 9. Summary of S_{Hmax} orientation in tectonic context. The blue lines are streamlines of estimated S_{Hmax} orientation. Background figure same as Figure 1a. The dots show locations of earthquake focal mechanisms.

Valley (Calais et al., 2010), or aftershocks from the 1811 to 1812 earthquakes (Stein & Liu, 2009). Many models of intraplate earthquakes incorporate a weak zone below the Reelfoot Rift (e.g., Grollimund & Zoback, 2001; Kenner & Segall, 2000), and if this were to exist, it might explain the slight rotations in S_{Hmax} across the central and eastern portions of the North American Craton and increased compression in the New Madrid and Wabash Valley Seismic Zones.

This study was undertaken to better understand the orientation of principal stresses in the Midcontinent. Such information is of value to effectively manage the risks associated with subsurface injection, including carbon sequestration efforts in the Illinois Basin (Lahann et al., 2017). Seismic events in response to fluid injection are not completely understood, particularly for basement faults located outside of the intended storage formation (Chang & Segall, 2016; Zhang et al., 2013). Pore pressures can propagate through fractures within the intended storage formation and into basement rock if there is no confining layer between the intended reservoir and the basement, leading to slip along faults optimally oriented with respect to the direction of maximum compressive stress (Chang & Segall, 2016; Zhang et al., 2013). The stress orientation information generated in this study could be useful for assessing the probability of fault slip as it relates to the angle of faults relative to S_{Hmax}. As shown by Darold and Holland (2015), ranking the risk of slip on mapped faults favorably oriented for reactivation with respect to the direction of maximum horizontal stress can be a useful tool for predicting potential fault slip and associated seismicity before, during, and after injection of fluid.

6. Conclusions

Stress field data for the Midcontinent were inverted to create a gridded array of maximum horizontal stress orientations. The damped-least stress inversion of Hardebeck and Michael (2006) was extended with the mixed linear/nonlinear Bayesian inversion scheme of Fukuda and Johnson (2010) to objectively estimate the degree of spatial smoothing, uncertainties in slip vectors, and the selection of nodal planes.

We find the stress field in the Midcontinent to be relatively homogenous. The regional trend of S_{Hmax} is ~N60°E; however, the maximum horizontal stress rotates clockwise to ~E-W across the southern Illinois Basin. Because the stress regime favors strike-slip faulting, the maximum horizontal stress (Figures 3 and 8b) is also the orientation of the maximum principal stress. Localized deviations from the regional trend of

S_{Hmax} orientation occur in the northeast corner of the New Madrid Seismic Zone and the Wabash Valley Seismic Zone. Also, in the northeast corner of the New Madrid and Wabash Valley Seismic Zones, we see a change in the dominant faulting style from strike-slip to reverse. This indicates that in this region, the most vertical principal stress alternates between the intermediate and minimum principal stresses.

Appendix A

To illustrate and validate the stress inversion with fault plane selection, we generate a synthetic focal mechanism data set and invert for stress tensor components in 2-D. First, the "true" stress state is assumed with most- and least-compressive principal stresses oriented as illustrated in Figure A1a. The intermediate principal stress is assumed to be perpendicular to the plane (plane stress), which is imagined to be a vertical cross section in this case. We then randomly place 100 focal mechanism centroids in the plane. The fault plane orientations at the 100 centroids are selected randomly from a Gaussian distribution with mean strike perpendicular to the plane with standard deviation of 60° and mean dip of 45° with standard deviation of 60°. Synthetic slip vectors are then constructed using equation (3) and the assumed fault orientations and stress state. The associated auxiliary nodal planes and slip vectors are also constructed as part of the synthetic data set, and no prior preference for the true fault plane or the auxiliary fault plane is provided. Random noise from a Gaussian distribution with standard deviation of 0.1 units is added to the true and auxiliary unit slip vectors. In the inversion, we assume the identity matrix for the data covariance matrix so that the estimated data weight, σ, should be the standard deviation of the noise added to the synthetic signal.

Figure A1b shows the estimated posterior distribution of principal stresses.

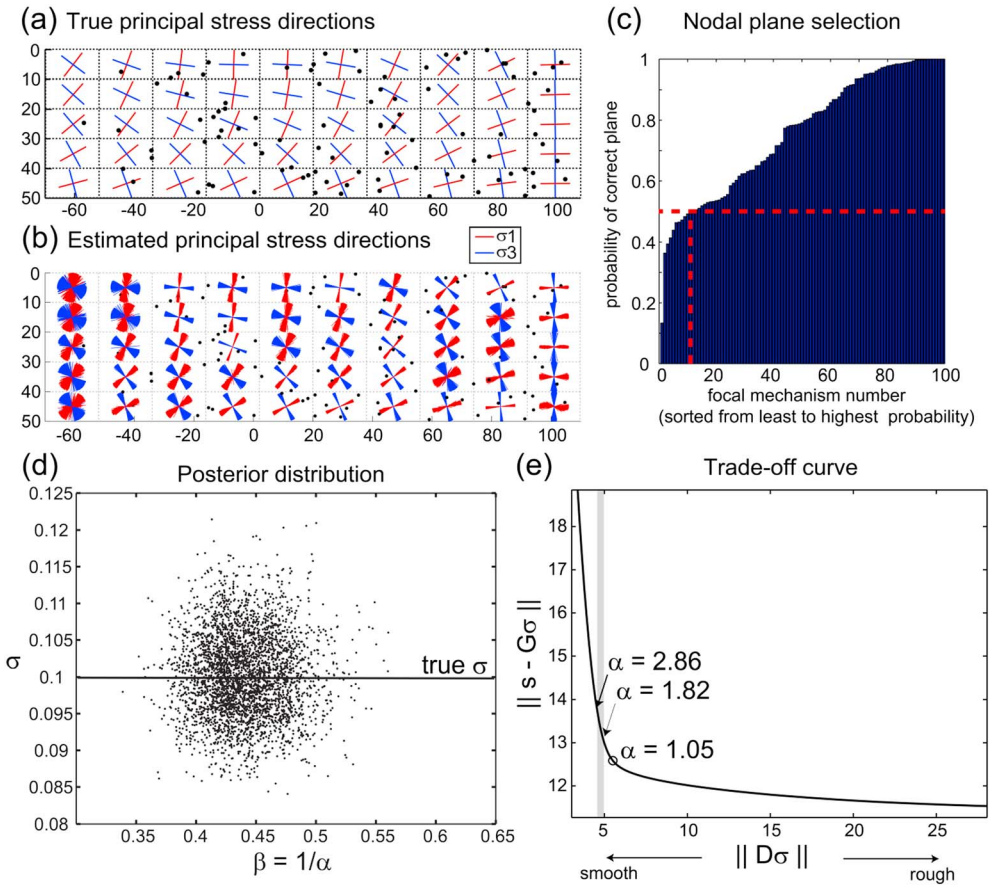

Figure A1. Results of synthetic stress inversion. (a) True principal stress directions. (b) Posterior distribution of principal stress directions. (c) Posterior probability of nodal plane. Plot shows probability that the true nodal plane is selected plotted in order from least to highest probability. (d) Joint posterior probability distribution of data weight, σ, and smoothing parameter, β. (e) Trade curve showing plot of misfit vs. roughness for different values of β. Gray vertical line is the Bayesian estimate.

To generate the posterior distributions of principal stress orientations, 1,000 stress states are selected from the posterior distribution of the stress tensor and the principal orientations of the 1,000stress tensors are computed and plotted. The true principal stresses (Figure A1a) lie within the posterior distributions, illustrating the ability of the inversion to recover the true values. Figure A1c shows the probability that the correct nodal plane was selected. The correct plane was selected more than 50% of the time for about 90% of the focal mechanisms, indicating that the inversion can usually identify the true fault plane. Figure A1d shows the joint posterior probability distribution of the data standard deviation, σ, and the smoothing parameter, β, as well as the true value of the data standard deviation.

Hardebeck and Michael (2006) use trade-off curves, a common approach in damped inversions, to select a smoothing parameter. Figure A1e compares the optimal smoothing parameter from our inversion with a trade-off curve. The trade-off curve plots the trade-off between the two vector norms minimized in equation (6). Recall that $\mathbf{D}$ is the first-derivative operator, and thus, $\|\mathbf{D}\sigma\|$ is a measure of spatial smoothness, and $\|\mathbf{s} - \mathbf{G}\sigma\|$ is a measure of misfit between observed, $\mathbf{s}$, and computed, $\mathbf{G}\sigma$, slip directions. Here we have introduced α, which is simply the inverse of smoothing parameter, β. To reduce computation time, this trade-off curve is computed with nodal planes fixed to the true fault planes. The optimal smoothing parameter from the Bayesian inversion is slightly smaller (corresponding to smoother stress state) than the value in the bend of the trade-off curve. However, the trade-off curve value is subjective in that the choice of parameters to plot in the trade-off curve is arbitrary and the geometry of the curve and the location of the bend in the curve will depend on the scaling of the plot (e.g., Fukuda & Johnson, 2008).

Acknowledgments
Focal mechanism data used in this study are obtained from various catalogs cited in the references and compiled in Table 1. In situ maximum horizontal stress orientation data used in this study are compiled in Table 2. We would like to thank Robert Bauer at the Illinois State Geological Survey for providing in situ maximum horizontal stress orientations from borehole breakout, hydrofracture, overcoring, and strain gauge measurements for the state of Illinois. This data set is noted in Table 2 as "New to Lahann et al. (2017)". Three of the borehole breakouts are from the Indiana Geological and Water Survey, Petroleum Data Management System (PDMS), https://igws.indiana.edu/PDMS/.

References

Anderson, E. M. (1905). The dynamics of faulting. *Transactions. Edinburgh Geological Society*, *8*(3), 387–402. https://doi.org/10.1144/transed.8.3.387

Anderson, E. M. (1951). *The dynamics of faulting and dyke formation with Applications to Britain* (2nd ed.). Edinburgh: Oliver and Boyd.

Angelier, J. (1979). Determination of the mean principal directions of stresses for a given fault population. *Tectonophysics*, *56*(3-4), T17–T26. https://doi.org/10.1016/0040-1951(79)90081-7

Angelier, J. (1984). Tectonic analysis of fault slip data sets. *Journal of Geophysical Research*, *89*(B7), 5835–5848. https://doi.org/10.1029/JB089iB07p05835

Angelier, J. (1990). Inversion of field data in fault tectonics to obtain the regional stress, III. A new rapid direct inversion method by analytical means. *Geophysical Journal International*, *103*(2), 363–376. https://doi.org/10.1111/j.1365-246X.1990.tb01777.x

Angelier, J., Tarantola, A., Valette, B., & Manoussis, S. (1982). Inversion of field data in fault tectonics to obtain the regional stress: I. Single phase fault populations: A new method of computing the stress tensor. *Geophysical Journal of the Royal Astronomical Society*, *69*(3), 607–621. https://doi.org/10.1111/j.1365-246X.1982.tb02766.x

Armijo, R., Carey, E., & Cisternas, A. (1982). The inverse problem in microtectonics and the separation of tectonic phases. *Tectonophysics*, *82*(1-2), 145–160. https://doi.org/10.1016/0040-1951(82)90092-0I

Arnold, R., & Townend, J. (2007). A Bayesian approach to estimating tectonic stress from seismological data. *Geophysical Journal International*, *170*(3), 1336–1356. https://doi.org/10.1111/j.1365-246X.2007.03485.x

Balfour, N. J., Savage, M. K., & Townend, J. (2005). Stress and crustal anisotropy in Marlborough, New Zealand: Evidence for low fault strength and structure-controlled anisotropy. *Geophysical Journal International*, *163*(3), 1073–1086. https://doi.org/10.1111/j.1365-246X.2005.02783.x

Bear, G. W. (1998). Integration of seismic reflection and potential field analysis: Architecture and Precambrian sedimentary basins in Indiana, Illinois, and Kentucky (Doctoral dissertation, Indiana University), 1–173.

Bott, M. H. P. (1959). The mechanics of oblique slip faulting. *Geological Magazine*, *96*(02), 109–117. https://doi.org/10.1017/S0016756800059987

Calais, E., Freed, A. M., Van Arsdale, R., & Stein, S. (2010). Triggering of New Madrid seismicity by late-Pleistocene erosion. *Nature*, *466*(7306), 608–611. https://doi.org/10.1038/nature09258

Carey, E., & Brunier, B. (1974). Numerical analysis of an elementary mechanical model applied to the study of a population of faults. *Comptes Rendus Hebdomadaires Des Seances De l'Academie Des Sciences. Serie D: Sciences Naturelles*, *279*, 891–894.

Chang, K. W., & Segall, P. (2016). Injection-induced seismicity on basement faults including poroelastic stressing. *Journal of Geophysical Research: Solid Earth*, *121*, 2708–2726. https://doi.org/10.1002/2015JB012561

Chen, C., Gilbert, H., Andronicos, C., Hamburger, M. W., Larson, T., Marshak, S., et al. (2016). Shear velocity structure beneath the central United States: Implications for the origin of the Illinois Basin and intraplate seismicity. *Geochemistry, Geophysics, Geosystems*, *17*(3), 1020–1041. https://doi.org/10.1002/2015GC006206

Couëslan, M. L., Smith, V., El-Kaseeh, G., Gilbert, J., Preece, N., Zhang, L., & Gulati, J. (2014). Development and implementation of a seismic characterization and CO_2 monitoring program for the Illinois Basin-Decatur Project. *Greenhouse Gases: Science and Technology*, *4*(5), 626–644. https://doi.org/10.1002/ghg.1452

Csontos, R., & Van Arsdale, R. (2008). New Madrid Seismic Zone fault geometry. *Geosphere*, *4*(5), 802–813. https://doi.org/10.1130/GES00141.1

Darold, A. P., & Holland, A. A. (2015). Preliminary Oklahoma optimal fault orientations, Oklahoma Geological Survey Open-File Report, OF4–2015.

Ekström, G., Nettles, M., & Dziewonski, A. M. (2012). The global CMT project 2004-2010: Centroid-moment tensors for 13,017 earthquakes. *Physics of the Earth and Planetary Interiors*, *200-201*, 1–9. https://doi.org/10.1016/j.pepi.2012.04.002

Etchecopar, A., Vasseur, G., & Daignieres, M. (1981). An inverse problem in microtectonics for the determination of stress tensors from fault striation analysis. *Journal of Structural Geology*, *3*(1), 51–65. https://doi.org/10.1016/0191-8141(81)90056-09

Fukuda, J., & Johnson, K. M. (2010). Mixed linear-non-linear inversion of crustal deformation data: Bayesian inference of model, weighting and regularization parameters. *Geophysical Journal International*, *181*(3), 1441–1458. https://doi.org/10.1111/j.1365-246X.2010.04564.x

Fukuda, J. I., & Johnson, K. M. (2008). A fully Bayesian inversion for spatial distribution of fault slip with objective smoothing. *Bulletin of the Seismological Society of America*, *98*(3), 1128–1146. https://doi.org/10.1785/0120070194

Gephart, J. W. (1990a). FMSI: A FORTRAN program for inverting fault/slickenside and earthquake focal mechanism data to obtain the regional stress tensor. *Computational Geosciences*, *16*(7), 953–989. https://doi.org/10.1016/0098-3004(90)90105-3

Gephart, J. W. (1990b). Stress and the direction of slip on fault planes. *Tectonics*, *9*(4), 845–858. https://doi.org/10.1029/TC009i004p00845

Gephart, J. W., & Forsyth, D. W. (1984). An improved method for determining the regional stress tensor using earthquake focal mechanism data: Application to the San Fernando earthquake sequence. *Journal of Geophysical Research*, *89*(B11), 9305–9320. https://doi.org/10.1029/JB089iB11p09305

Gomberg, J. (1993). Tectonic deformation in the New Madrid Seismic Zone: Inferences from map view and cross-sectional boundary element models. *Journal of Geophysical Research*, *98*(B4), 6639–6664. https://doi.org/10.1029/92JB02857

Gomberg, J. S. (1992). Tectonic deformation in the New Madrid Seismic Zone: Inferences from boundary element modeling. *Seismological Research Letters*, *63*, 407–425.

Grollimund, B., & Zoback, M. D. (2001). Did deglaciation trigger intraplate seismicity in the New Madrid Seismic Zone? *Geology*, *29*(2), 175–178. https://doi.org/10.1130/0091-7613(2001)029%3C0175:DDTISI%3E2.0.CO;2

Hamburger, M. W., & Rupp, J. (1988). The June 1987 southeastern Illinois earthquake: Possible tectonism associated with the La Salle anticlinal belt. *Seismological Research Letters*, *59*, 151–158.

Hamburger, M. W., Shoemaker, K., Horton, S., DeShon, H., Withers, M., Pavlis, G. L., & Sherrill, E. (2011). Aftershocks of the 2008 Mt. Carmel, Illinois, earthquake: Evidence for conjugate faulting near the termination of the Wabash Valley fault system. *Seismological Research Letters*, *82*(5), 735–747. https://doi.org/10.1785/Gssrl.82.5.735

Hardebeck, J. L., & Hauksson, E. (2001a). Crustal stress field in southern California and its implications for fault mechanics. *Journal of Geophysical Research*, *106*(B10), 21,859–21,882. https://doi.org/10.1029/2001JB000292

Hardebeck, J. L., & Hauksson, E. (2001b). Stress orientations obtained from earthquake focal mechanisms: What are appropriate uncertainty estimates? *Bulletin of the Seismological Society of America*, *91*(2), 250–262. https://doi.org/10.1785/0120000032

Hardebeck, J. L., & Michael, A. J. (2006). Damped regional-scale stress inversions: Methodology and examples for southern California and the Coalinga aftershock sequence. *Journal of Geophysical Research: Solid Earth*, *111*, B11310. https://doi.org/10.1029/2005JB004144

Herrmann, R. B., Benz, H., & Ammon, C. J. (2011). Monitoring the earthquake process in North America. *Bulletin of the Seismological Society of America*, *101*, 2809–2625. https://doi.org/10.1785/0120110095

Hurd, O., & Zoback, M. D. (2012a). Intraplate earthquakes, regional stress and fault mechanics in the Central and Eastern U.S. and Southeastern Canada. *Tectonophysics*, *581*, 182–192. https://doi.org/10.1016/j.tecto.2012.04.002

Hurd, O., & Zoback, M. D. (2012b). Regional stress orientations and slip compatibility of earthquake focal planes in the New Madrid Seismic Zone. *Seismological Research Letters*, *83*(4), 672–679. https://doi.org/10.1785/0220110122

Indiana Geological and Water Survey (2015). Petroleum Database Management System, accessed June 15, 2015. https://igws.indiana.edu/PDMS/

Johnston, A. C., & Schweig, E. S. (1996). The enigma of the New Madrid earthquakes of 1811–1812. *Annual Review of Earth and Planetary Sciences*, *24*(1), 339–384. https://doi.org/10.1146/annurev.earth.24.1.339

Kastrup, U., Zoback, M. L., Deichmann, N., Evans, K. F., Giardini, D., & Michael, A. J. (2004). Stress field variations in the Swiss Alps and the northern Alpine foreland derived from inversion of fault plane solutions. *Journal of Geophysical Research*, *109*, B01402. https://doi.org/10.1029/2003JB002550

Kaven, J. O., Hickman, S. H., McGarr, A. F., & Ellsworth, W. L. (2015). Surface monitoring of microseismicity at the Decatur, Illinois, CO_2 sequestration demonstration site. *Seismological Research Letters*, *86*(4), 1096–1101. https://doi.org/10.1785/0220150062

Kelson, K. I., Simpson, G. D., Lettis, W., Vanarsdale, R. B., Haraden, C. C., & Lettis, W. R. (1996). Multiple late Holocene earthquakes along the Reelfoot fault, central New Madrid Seismic Zone. *Journal of Geophysical Research*, *101*(B3), 6151–6170. https://doi.org/10.1029/95JB01815

Kenner, S. J., & Segall, P. (2000). A mechanical model for intraplate earthquakes: Application to the New Madrid Seismic Zone. *Science*, *289*(5488), 2329–2332. https://doi.org/10.1126/science.289.5488.2329

Keranen, K. M., Savage, H. M., Abers, G. A., & Cochran, E. S. (2013). Potentially induced earthquakes in Oklahoma, USA: Links between wastewater injection and the 2011 Mw 5.7 earthquake sequence. *Geology*, *41*(6), 699–702. https://doi.org/10.1130/G34045.1

Kim, W. Y. (2013). Induced seismicity associated with fluid injection into a deep well in Youngstown, Ohio. *Journal of Geophysical Research: Solid Earth*, *118*(7), 3506–3518. https://doi.org/10.1002/jgrb.50247

Lahann, R. L., Rupp, J. A., Medina, C. R., Carlson, G., & Johnson, K. M. (2017). State of stress in the Illinois Basin and constraints on inducing failure. *AAPG Environmental Geosciences*, *24*(3), 123–150. https://doi.org/10.1306/eg.0206171600817004

Mazzotti, S., & Townend, J. (2010). State of stress in central and eastern North American seismic zones. *Lithosphere*, *2*(2), 76–83. https://doi.org/10.1130/L65.1

McKenzie, D. P. (1969). The relation between fault plane solutions for earthquakes and the directions of the principal stresses. *Bulletin of the Seismological Society of America*, *59*, 591–601.

Michael, A. J. (1984). Determination of stress from slip data: Faults and folds. *Journal of Geophysical Research*, *89*(B13), 11,517–11,526. https://doi.org/10.1029/JB089iB13p11517

Michael, A. J. (1987a). Use of focal mechanisms to determine stress: A control study. *Journal of Geophysical Research*, *92*(B1), 357–368. https://doi.org/10.1029/JB092iB01p00357

Michael, A. J. (1987b). Stress rotation during the Coalinga aftershock sequence. *Journal of Geophysical Research*, *92*(B8), 7963–7979. https://doi.org/10.1029/JB092iB08p07963

Michael, A. J. (1991). Spatial variations in stress within the 1987 Whittier Narrows, California, aftershock sequence: New technique and results. *Journal of Geophysical Research*, *96*, 6303–6319.

Nelson, W. J. (1991). Structural styles in the Illinois Basin. In M. W. Leighton, et al. (Eds.), *Interior Cratonic Basins: AAPG Memoir* (Vol. 51, pp. 209–243).

Nuttli, O. W. (1979). Seismicity of the central United States. *Geological Society of America Review Engineering Geology*, 67–93.

Pavlis, G. L., Rudman, A. J., Pope, B. M., Hamburger, M. W., Bear, G. W., & Al-Shukri, H. (2002). Seismicity of the Wabash Valley Seismic Zone based on a temporary seismic array experiment. *The Illinois Basin; Seismicity, Quaternary Faulting, and Seismic Hazard*, *73*(5), 751–761. https://doi.org/10.1785/gssrl.73.5.751

Pollitz, F. F., & Mooney, W. D. (2013). Seismic structure of the central US crust and shallow upper mantle: Uniqueness of the Reelfoot Rift. *Earth and Planetary Science Letters*, *402*(C), 157–166.

Reches, Z. (1987). Determination of the tectonic stress tensor from slip along faults that obey the Coulomb yield condition. *Tectonics*, *6*(6), 849–861. https://doi.org/10.1029/TC006i006p00849

Sherburn, S., & White, R. S. (2005). Crustal seismicity in Taranaki, New Zealand using accurate hypocentres from a dense network. *Geophysical Journal International*, *162*(2), 494–506. https://doi.org/10.1111/j.1365-246X.2005.02667.x

Simpson, R. W. (1997). Quantifying Anderson's fault types. *Journal of Geophysical Research*, *102*(B8), 17909–17919. https://doi.org/10.1029/97JB01274

Soderberg, R. K., & Keller, G. R. (1981). Geophysical evidence for deep basin in western Kentucky. *American Association of Petroleum Geologists Bulletin*, *65*(2), 226–234.

Stein, S., & Liu, M. (2009). Long aftershock sequences within continents and implications for earthquake hazard assessment. *Nature*, *462*(7269), 87–89. https://doi.org/10.1038/nature08502

Tuttle, M. P. (2001). The use of liquefaction features in paleoseismology: Lessons learned in the New Madrid Seismic Zone, central United States. *Journal of Seismology*, *5*(3), 361–380. https://doi.org/10.1023/A:1011423525258

Tuttle, M. P., & Schweig, E. S. (1996). Recognizing and dating prehistoric liquefaction features: Lessons learned in the New Madrid Seismic Zone, central United States. *Journal of Geophysical Research*, *101*(B3), 6171–6178. https://doi.org/10.1029/95JB02894

van der Baan, M., & Calixto, F. J. (2017). Human-induced seismicity and large-scale hydrocarbon production in the USA and Canada. *Geochemistry, Geophysics, Geosystems*, *18*(7), 2467–2485. https://doi.org/10.1002/2017GC006915

Vavryčuk, V. (2014). Iterative joint inversion for stress and fault orientations from focal mechanisms. *Geophysical Journal International*, *199*(1), 69–77. https://doi.org/10.1093/gji/ggu224

Wallace, R. E. (1951). Geometry of shearing stress and relation to faulting. *Journal of Geology*, *59*(2), 118–130. https://doi.org/10.1086/625831

World Stress Map (2015). Stress data of the WSM, accessed June 15, 2015. Retrieved from http://dc-app3-14.gfz-potsdam.de/pub/stress_data/stress_data_frame.html

Yang, X., Pavlis, G. L., Hamburger, M. W., Sherrill, E., Gilbert, H., Marshak, S., et al. (2014). Seismicity of the Ste. Genevieve Seismic Zone based on observations from the EarthScope OIINK Flexible Array. *Seismological Research Letters*, *85*(6), 1285–1294. https://doi.org/10.1785/0220140079

Yang, Y. R., Johnson, K. M., & Chuang, R. Y. (2013). Inversion for absolute deviatoric crustal stress using focal mechanisms and coseismic stress changes: The 2011 M9 Tohoku-oki, Japan, earthquake. *Journal of Geophysical Research: Solid Earth*, *118*(10), 5516–5529. https://doi.org/10.1002/jgrb.50389

Yeck, W. L., Hayes, G. P., McNamara, D. E., Rubinstein, J. L., Barnhart, W. D., Earle, P. S., & Benz, H. M. (2016). Oklahoma experiences largest earthquake during ongoing regional wastewater injection hazard mitigation efforts. *Geophysical Research Letters*, *44*, 711–717. https://doi.org/10.1002/2016GL071685

Zhang, Y., Person, M., Rupp, J., Ellett, K., Celia, M. A., Gable, C. W., et al. (2013). Hydrogeologic controls on induced seismicity in crystalline basement rocks due to fluid injection into basal reservoirs. *Ground Water*, *51*(4), 525–538. https://doi.org/10.1111/gwat.12071

Zoback, M. (2007). In *Reservoir Geomechanics* (pp. 165–166), Cambridge: Cambridge University Press.

Zoback, M. L. (1992). Stress field constraints on intraplate seismicity in eastern North America. *Journal of Geophysical Research*, *97*(B8), 11,761–11,782. https://doi.org/10.1029/92JB00221

Zoback, M. L., & Zoback, M. (1980). State of stress in the conterminous United States. *Journal of Geophysical Research*, *85*(B11), 6113–6156. https://doi.org/10.1029/JB085iB11p06113

Zoback, M. L., & Zoback, M. D. (1989). Tectonic stress field of the continental United States. In L. C. Pakiser & W. D. Mooney (Eds.), *Geophysical framework of the continental United States* (p. 172). Boulder, CO: Geological Society of America Memoir.